Effect of ice particles on the mesospheric potassium layer at Spitsbergen (78°N)

Shikha Raizada,[1,2] Markus Rapp,[1] F.-J. Lübken,[1] J. Höffner,[1] M. Zecha,[1] and J. M. C. Plane[3,4]

[1] This paper quantitatively evaluates the influence of ice particles on the K layer by using radar and lidar measurements. The methodology involves determination of the volumetric surface area $[A_{ice}]$ of the ice particles in a noctilucent cloud by combining a microphysical ice particle model with a charging model to produce an empirical proxy for polar mesosphere summer echoes (PMSE) based on the properties of the charged aerosol particles. The altitudinal variation of $[A_{ice}]$ reveals peak values of about 2.2×10^{-8} cm^{-1} around 85 km. The first-order loss rate of atomic K due to uptake on the ice particles maximizes close to 2.2×10^{-4} s^{-1} at 85 km. To examine the variability of $[A_{ice}]$ on background parameters, a sensitivity study showed that a ±10% variation in $[A_{ice}]$ can result from either a ±5 K shift in the temperatures relative to a background profile or from a ±30% change in the water vapor concentration. We found that the peak $[A_{ice}]$ remains constant for a change of +4 to −6 K temperature fluctuations over the altitude range of 83–85 km. Finally, a new atmospheric model of potassium predicts profiles of the K layer in early May and July that are in good agreement with the observations, when the seasonally averaged K ablation flux at 79°N is set to 160 atom cm^{-2} s^{-1}. This study reveals that both the vertical wind and ice particles play a significant role in controlling the K layer distribution at high latitudes.

1. Introduction

[2] Ablation of meteoroids results in the deposition of various metallic species in the 80 – 110 km region of the Earth's mesosphere. These act as tracers for studying the chemistry and dynamics of this region [e.g., *Plane*, 2003]. One of the characteristics of this part of the mesosphere is the occurrence of very low temperatures during the summer [*Lübken*, 1999]. Such low temperatures are favorable for the growth of ice particles between 80–90 km altitude, even though water vapor is a minor constituent with typical volume mixing ratios of a few ppm. These ice particles manifest in the form of noctilucent clouds (NLC) which can be optically observed owing to their larger size (radii > 30 nm). These and smaller ice particles (radii > 3 nm) are responsible for strong radar echoes in the VHF wavelength range, referred to as polar mesosphere summer echoes (PMSE) (see *Thomas* [1991] and *Rapp and Lübken* [2004] for suitable reviews).

[3] A lot of observational and theoretical effort has gone into the understanding of the physical mechanism of PMSE generation [*Kelley et al.*, 1987; *Cho et al.*, 1992; *Cho and Röttger*, 1997; *Hocking and Röttger*, 1997; *Balsley and Huaman*, 1997; *Blix et al.*, 2003; *Chilson et al.*, 2000; *Rapp and Lübken*, 2000; *Rapp and Lübken*, 2004, and references therein]. This interest arose partly because of the paradox presented by the occurrence of the radar Bragg scale (~3 m for 50 MHz radar) in the viscous subrange of the neutral turbulence power spectrum, the region where irregularities are destroyed by molecular diffusion. Later on, it was shown that mesospheric neutral air turbulence in combination with reduced electron diffusivity due to the presence of heavy charged ice aerosol particles can create structures with scales smaller than the inner scale of the neutral gas turbulent velocity field [*Kelley et al.*, 1987, *Cho et al.*, 1992]. The reduction of electron diffusivity in the presence of aerosol particles and the charging of the latter due to the diffusional fluxes of electrons onto their surface are recognized as major physical processes causing PMSE [*Cho et al.*, 1992; *Rapp and Lübken*, 2003].

[4] As a further step, *Rapp et al.* [2003] combined models of ice particle microphysics and aerosol charging that allowed simulations of both neutral and charged aerosol species to test the idea that the general characteristics of PMSE can be explained by properties of charged aerosols. This led to the development of an empirical 'Proxy' for PMSE given by

$$\text{PMSE} \propto (|Z_A|N_A)r_A^2 = \text{Proxy}$$

[1]Institute of Atmospheric Physics, Kühlungsborn, Germany.
[2]Now at Arecibo Observatory, Arecibo, Puerto Rico, USA.
[3]School of Environmental Sciences, University of East Anglia, Norwich, UK.
[4]Now at School of Chemistry, University of Leeds, Leeds, UK.
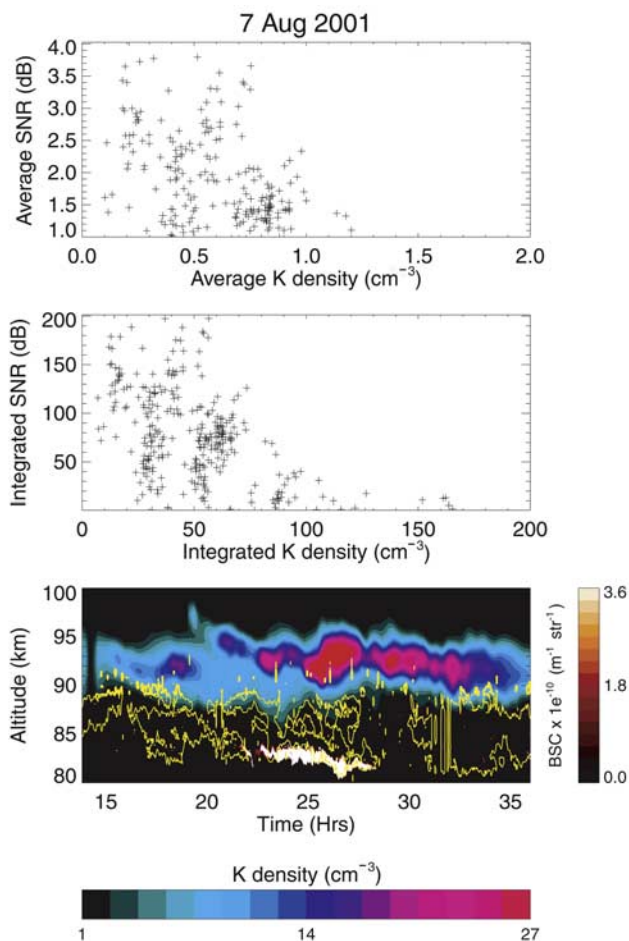
Figure 1. (bottom) Spatial and temporal variation of the potassium layer (shown as colored contour) obtained using a resonance lidar from Spitsbergen. Also superimposed are the yellow contour lines for signal-to-noise ration (SNR) corresponding to polar mesosphere summer echoes (PMSE) observed using collocated Sousy radar along with the noctilucent clouds (NLC) contours (filled). (center) Scatterplot of column-integrated K densities and SNR in the regions of overlap, demonstrating a decrease in the total K densities when the PMSE strength is greater. (top) Similar to Figure 1, center, except showing the variation of the average PMSE and K densities in the overlap region.

where, $|Z_A|$ is the number of elementary charges per particle, N_A is the particle number density and r_A is the radius of the particles. The dependence on the square of particle radius comes from the fact that the aerosol diffusion coefficient varies as the inverse of r_A^2 [*Cho et al.*, 1992].

[5] Recently, others have found evidence of the effect of these ice particles on metal atoms [*Plane et al.*, 2004; *Lübken and Höffner*, 2004; *She et al.*, 2006; *Gardner et al.*, 2005]. Modeling studies have explained the complete removal of atomic Fe by uptake on ice in the altitude range that overlaps with the NLC at South Pole [*Plane et al.*, 2004]. Importantly, the model simulations were based on laboratory experiments performed at mesospheric temperatures of 130–150 K to measure the uptake rate of Fe on

cubic crystalline ice [*Murray and Plane*, 2005b]. Such studies reveal that the uptake coefficient (γ), which is the probability that metal atoms colliding with the ice surface are permanently removed from the gas phase, is close to unity for Fe, Na and K.

[6] The various mesospheric metal species respond differently to atmospheric background conditions and constituents [*Plane*, 2003]. Hence previous modeling of the influence of ice particles on the Na and Fe layers [*Plane et al.*, 2004; *Gardner et al.*, 2005] should now be extended to the K layer. Indeed, in this paper we present an experimental and modeling investigation of the impact of ice particles on the mesospheric K layer at polar latitudes. An important development here over previous work is that we used both lidar measurements of NLC and radar measurements of PMSE to estimate the volumetric surface area of the ice particles ([A_{ice}] defined as surface area of ice particles per unit volume), the parameter that is crucial for determining the rate of removal of the K species. The manuscript is organized as follows. The motivation and observations are discussed in Section 2, which is followed by the development of a semiempirical method for the determination of [A_{ice}] discussed in Section 3. In Section 4, we estimate the loss rate of K atoms during the peak NLC/PMSE season using [A_{ice}]. Section 5 presents a new time-resolved model of the K layer, which uses as input the results from Sections 3 and 4. Finally, we discuss our results and future work in the Sections 6 and 7.

2. Motivation and Observations

[7] Simultaneous lidar observations of NLC and radar measurements of PMSE were made at Spitsbergen (78°N) during the years 2001–2003 and suggested the influence of ice particles on the K layer [*Lübken et al.*, 2004; *Lübken and Höffner*, 2004]. The striking difference in the distribution of K at high latitudes as compared to other sites like Kühlungsborn (54°N) is the depletion of atoms from altitudes below 88 km during summertime at polar latitudes [*Lübken and Höffner*, 2004].

[8] Figure 1, bottom, shows a typical altitude and time variation of the K density at Spitsbergen along with signal-to-noise ratio (SNR) values from PMSE that are displayed as yellow contour lines. Also superimposed is the temporal and spatial variation of backscattering coefficients (BSC) corresponding to NLC for the same time interval. It is interesting to note that the upper edge of the PMSE often overlaps with the lower portion of the K layer. In order to evaluate the effect of PMSE on K on short timescales of just a few hours, we identified such overlap areas and calculated the average and integrated K densities and SNR in these regions. The scatterplot of column integrated K densities and SNR in the overlap regions along with their averages shown in Figure 1, top, reveals that the envelope of all points exhibits a decreasing trend of K densities with increasing SNR. Even though the observed trend shows a large scatter, it provides strong evidence that PMSE (and hence ice particles) reduce the K density, leading to signatures which can be clearly recognized on short timescales of just a few hours. This corroborates the earlier findings of *Lübken and Höffner* [2004] who concluded for the same
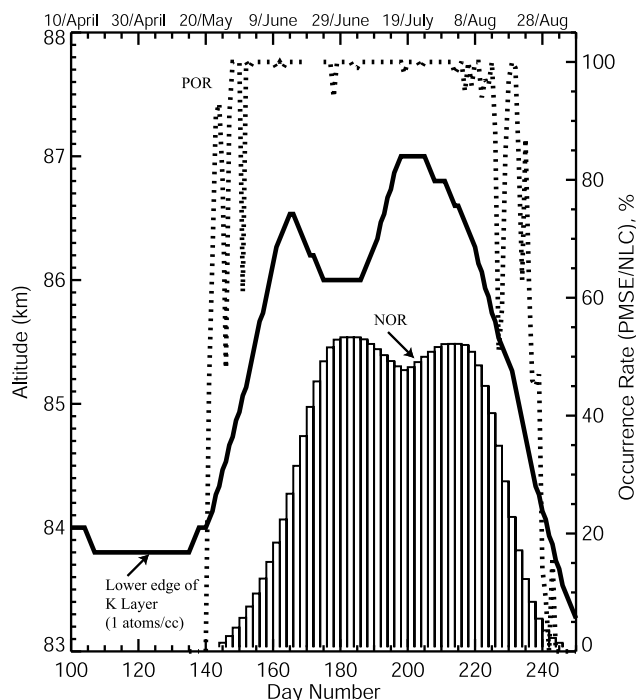
Figure 2. (solid line) Seasonal variation of the lower edge of the potassium layer with altitude. It clearly shows the displacement of the lower edge to higher altitudes during June/July months during summertime. (dotted line) Occurrence rate of PMSE that is nearly 100% during peak summer. Histogram displays the peak occurrence rate of NLC at Spitsbergen, which maximizes during summertime also suggesting a correlation between ice particles and removal of K densities at lower altitudes on annual scale.

effect on the basis of their comparison of the seasonal variation of the K layer and PMSE.

[9] Figure 2 displays the variation of the lower edge of the K layer (defined as the minimum altitude where the K densities are just above detection threshold of 1 cm^{-3}) at Spitsbergen along with the PMSE occurrence rate (POR) (shown as dashed line) for the period 15 July to 31 August 2001. The NLC occurrence rate (NOR) is also displayed as the histogram peaking below 60%. It is interesting to note that the lower edge of the K layer moves upward by approximately 3 km during the peak PMSE season relative to the period just before the onset of PMSE (around mid-May). Also, it is worth noting that the occurrence rate of PMSE is nearly 100% during the peak season when the altitude of the lower edge of the K layer is highest. The removal of K densities during summertime from altitudes below 88 km has been qualitatively attributed to the presence of ice particles [*Lübken and Höffner*, 2004]. The aim of this work is to quantitatively investigate the dependence of the K density distribution at altitudes below ~90 km on PMSE/NLC.

3. An Empirical Approach for the Estimation of Volumetric Surface Areas of Ice Particles

[10] Our methodology consists of using PMSE and NLC data to infer the volumetric surface area corresponding to

the ice particles at mesospheric altitudes by using a combination of a microphysical ice model, CARMA (Community Aerosol and Radiation Model for Atmospheres) and a charging model [*Rapp and Thomas*, 2006; *Rapp and Lübken*, 2001; *Rapp et al.*, 2003]. This will be referred to as 'ECARMA' (Extension of CARMA). ECARMA allows us to calculate a proxy for PMSE, introduced in Section 1. *Rapp et al.* [2003] showed that the proxy matches very well with the observed mean PMSE profiles and recently, *Hoffmann et al.* [2005] succeeded to explain the occurrence of multilayer PMSE by model studies using ECARMA and considering the influence of long-period gravity waves. So, we proceeded with averaging the PMSE profiles from Spitsbergen for June–July (peak season), when the occurrence rate of ice particles is high. The altitude profiles of the averaged SNR and BSC corresponding to PMSE and NLC observed from Spitsbergen during the peak season are shown in Figure 3. The SNR maximizes around 85 km while lidar observed BSC peaks at ~83.5 km, the difference in height being the result of different scattering mechanisms which strongly depend on the size of the particles.

[11] The outputs from ECARMA were obtained for several cases centered on the mean background profiles representing June/July conditions at 78°N. Figure 4 displays the background parameters representing the mean climatological summer conditions around solstice that were used as input to ECARMA. Temperature and winds have been adapted from *Berger and von Zahn* [2002], the eddy diffusion profile is from *Lübken* [1997] (for summer conditions), and the water vapor profile from *Körner and Sonnemann* [2001]. The model produces mesopause temperatures ~120 K at 90 km, which is consistent with in situ observations by *Lübken and Müllemann* [2003]. The modeled water vapor profiles reveal values close to 2.5 ppmv at 85 km, which is in close agreement with microwave
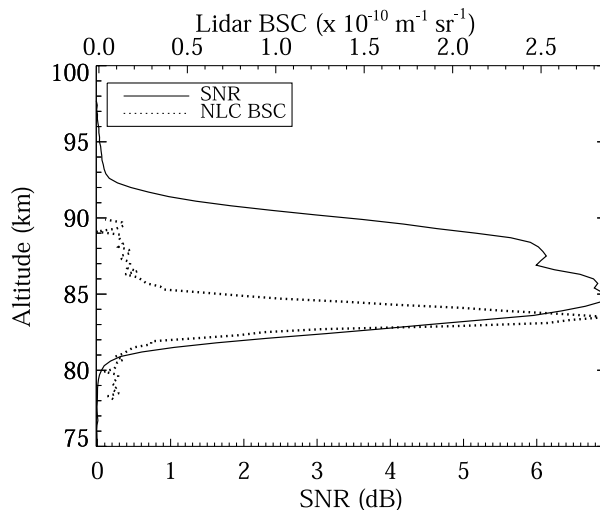
Figure 3. Altitudinal variation of averaged SNR and lidar-observed backscattering coefficients (BSC) for the peak NLC/PMSE season that have been used for the calculation of volumetric surface areas of ice particles. It can be seen that the lower edge of both PMSE and NLC overlap in altitude; however, their peaks display an offset of 1.5 km.
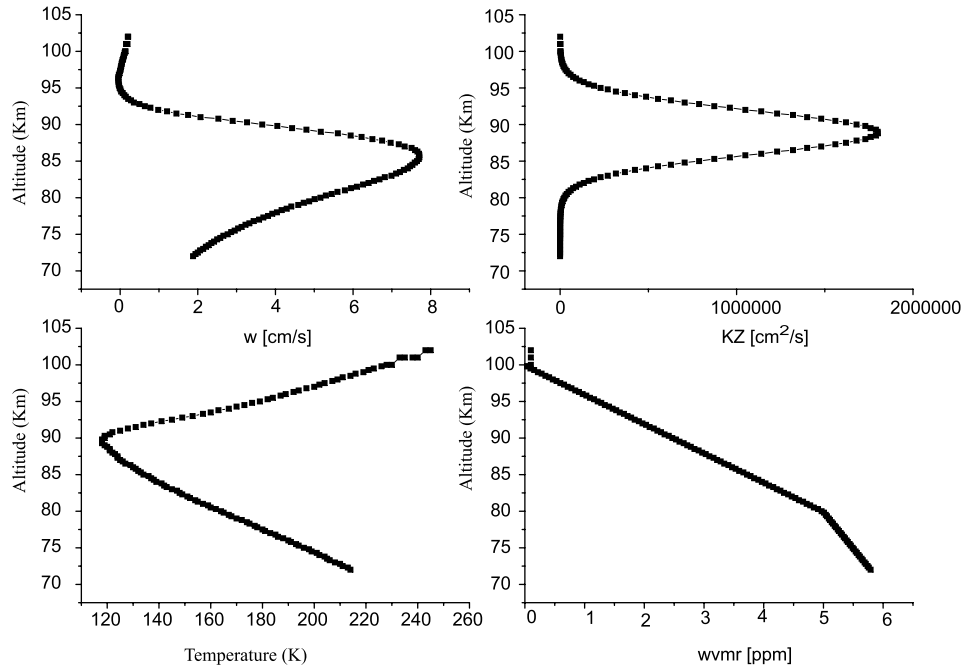
Figure 4. Altitudinal variation of background parameters that have been used as input to CARMA. (top) Vertical wind (w) and eddy diffusion (K_z); (bottom) temperature and water vapor mixing ratio (wvmr). The sensitivity studies were done using various shifts or factors to perturb these background profiles. Please see the text for more details.

measurements [*Seele and Hartogh*, 1999] but falls slightly short of satellite-borne estimates of the water vapor mixing ratio at these altitudes which yield values of ~4–5 ppmv [*McHugh et al.*, 2003].

[12] Next, we compared the modeled and observed BSC at 770 nm and their altitudinal variation can be seen in Figure 5a. It is evident that in both cases the BSC peaks around 83.5 km with values ~2.6 × 10^{-10} m^{-1} sr^{-1}. This study demonstrates that modeled and observed BSC are within ±10% of each other. The lidar observations from the year 2001–2003 show that the mean backscatter coefficient (BSC) due to NLC displays an annual variability of <15% [*Lübken et al.*, 2002]. Hence taking into account this year-to-year variability of the NLCs observations, we obtain a satisfactory match between model and observations. Figure 5b shows that the difference between the peak altitudes of SNR and proxy for the above selected case is less than 0.5 km, again implying a good match between observations and model. The slight mismatch between proxy and SNR above the peak is most likely due to the effect of gravity waves that has not been taken into account in the model calculation because we consider mean conditions.

[13] We found an empirical relationship between the selected proxy and the observed SNR by fitting a least squares best fit between the two sets that are shown in Figure 5c. Since ECARMA gives the characteristics of the ice particles, i.e., radius and volumetric surface areas, one can determine the latter corresponding to the observed PMSE by using the empirical relationship between proxy and SNR. Figure 5d displays the altitudinal distribution of the volumetric surface area [A_{ice}] of the ice particles that peaks close to 85 km with a value ~2.2 × 10^{-8} cm^{-1}. At

altitudes greater than 88 km, [A_{ice}] decreases by more than 41% relative to peak values.

4. Determination of K Uptake on Ice Using Lidar, PMSE Observations, and CARMA Model

4.1. Loss Rate of Potassium on Ice

[14] The mesospheric metal density depends on various sources and sinks that govern the production and loss mechanisms. Understanding the annual behavior of any species requires knowledge of how these different sources or sinks contribute. Considering the experimental evidence of the effect of ice particles on the seasonal distribution of mesospheric K, we evaluate quantitatively the role of ice particles as one of the major sinks using [A_{ice}] determined in Section 3. The loss of K density per unit time as a result of uptake on ice can be expressed as

$$L_{k\_ice} = \frac{1}{4}\left(\bar{u}\,\gamma\,[A_{ice}]\,[K_{unp}]\right)$$

where γ is the uptake coefficient, û is the mean velocity of K atoms, [A_{ice}] represents the volumetric surface area of ice particles and [K_{unp}] is the unperturbed K density. We note that this expression provides an upper estimate of the loss rate. With evolving time, the initial loss will reduce the potassium density which in turn will also result in a reduction of the instantaneous loss rate. For the full time-dependent treatment of the uptake process, the reader is referred to section 5.

[15] One of the difficulties in determining the loss rate is to estimate the mean unperturbed K density profile. We have considered the early May period to be representative of
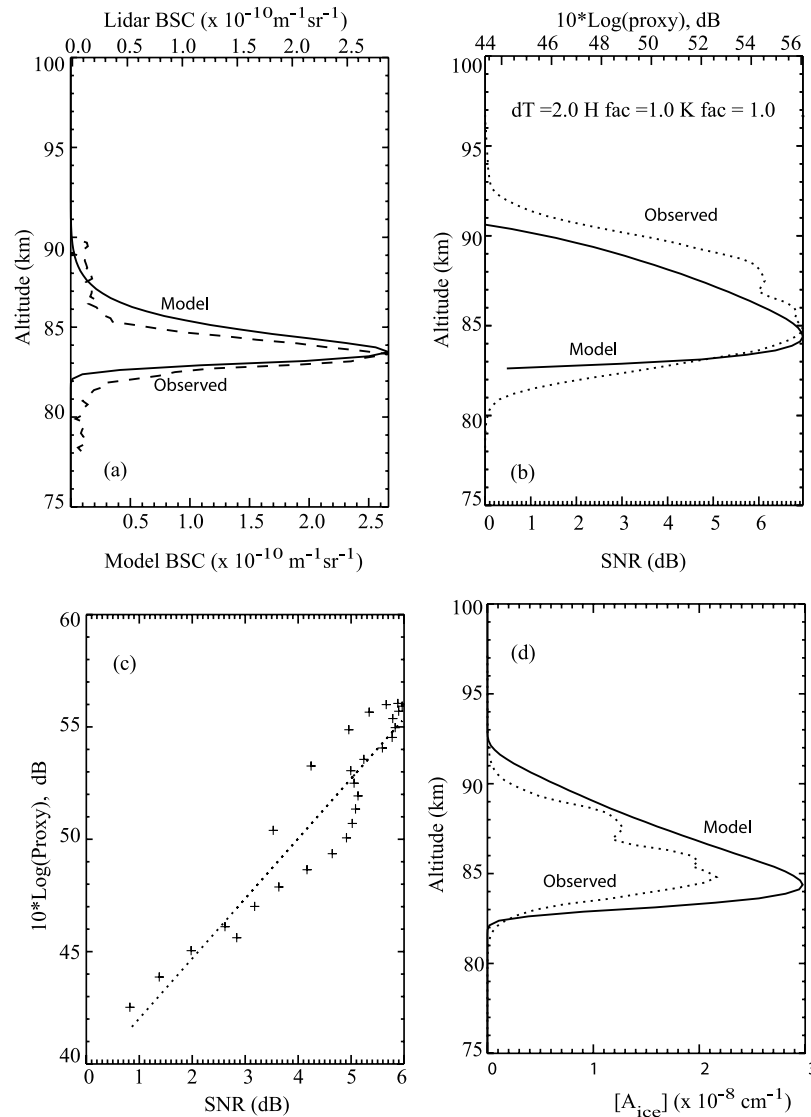
Figure 5. (a) Modeled and observed BSC are compared, depicted as solid and dashed lines, respectively. (b) Comparison between proxy and SNR for background conditions that produces a good match between the two, indicating that the choice of background parameters is reasonable. SNR has been obtained by averaging June/July PMSE data and represents average behavior at Spitsbergen. (c) Best square fit between the proxy and SNR. (d) Calculated volumetric surface areas corresponding to PMSE (dashed line) and the model (solid line).

the unperturbed conditions as it is the period just before the onset of the PMSE season. This is justified because at midlatitudes like Kühlungsborn (54°N), where the occurrence of NLC and PMSE is much less compared to high latitudes, the K density exhibits little seasonal variation [see *Lübken and Höffner,* 2004, Figure 1]. This choice of early May for the unperturbed profile provides a test of the hypothesis that the removal of mesospheric K below 87 km as observed in the seasonal variation of the lower edge of the K layer is primarily due to the presence of ice particles rather than other chemical sinks.

[16] In order to obtain the unperturbed profile, we averaged 10 days of K density centered on 5 May. Figure 6, left, shows the averaged K density profile, K_{per}, from the peak NLC/PMSE (core) season and the unperturbed K density

variation. It is evident that (1) K has been removed substantially and (2) during the core season K density peaks at nearly 93 km approximately 2 km higher than the non-PMSE season. This change in the peak altitude is very similar to that observed in the case of the Na and Fe layers at the South Pole [*Plane et al.,* 2004; *Gardner et al.,* 2005]. Figure 6, center, exhibits the altitude variation of the difference profile ($K_{unp} - K_{per}$) and loss rate of K atoms due to uptake on ice (L_{k_ice}). A very good correlation is seen between the difference profile and L_{k_ice} (except for a slight mismatch in peak altitude), indicating that the contribution of the ice particles cannot be neglected in explaining the seasonal behavior of the K layer. In addition, the difference profile shows a second altitude range with significantly larger K densities in May as compared to
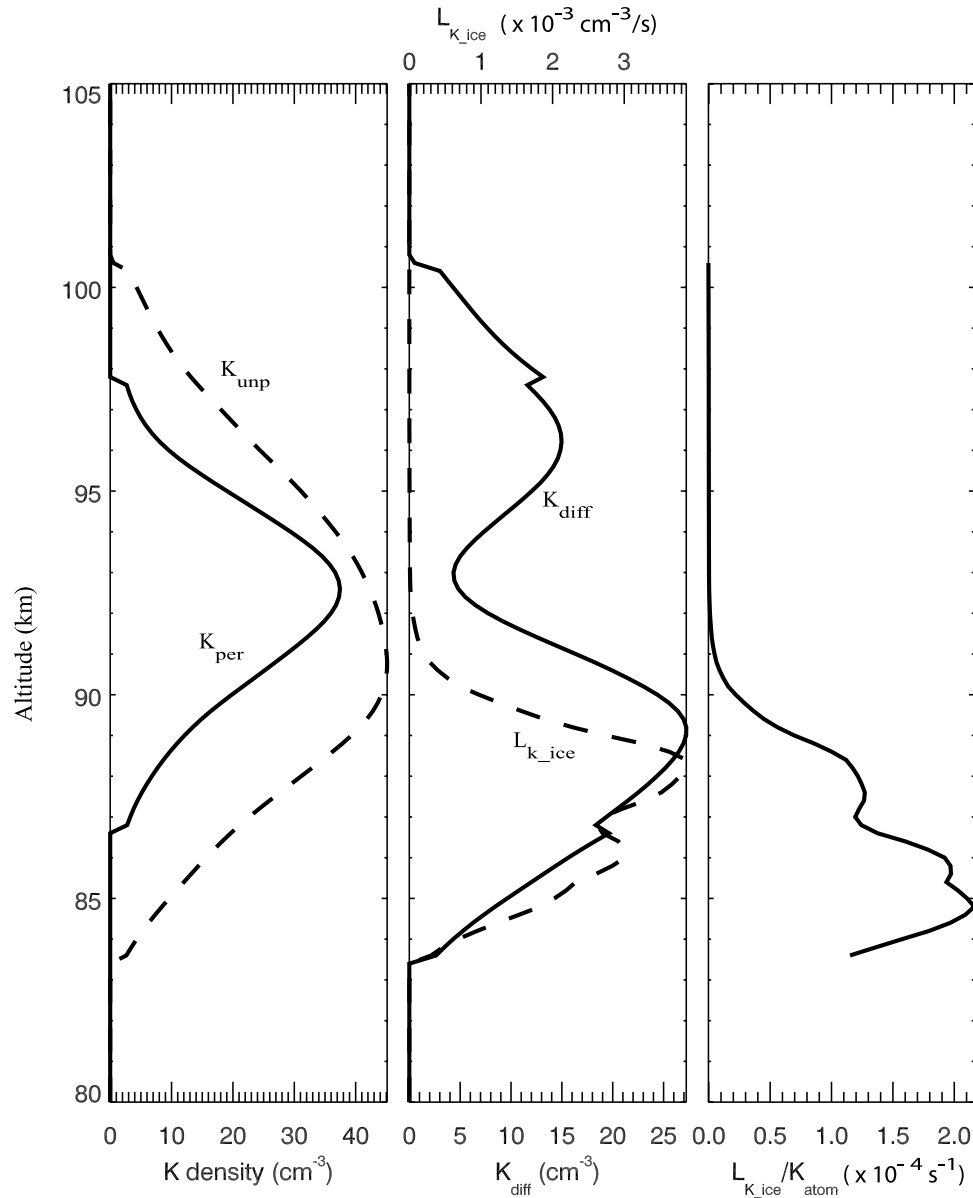
Figure 6. (left) Perturbed and unperturbed potassium density profile obtained from June/July and early May periods. The lower edge of the K layer during the peak summer period is shifted by ∼3 km relative to early May. (center) Altitudinal variation of the difference profile (K_{diff}, obtained by subtracting the two profiles shown in Figure 6, left) along with loss rate of K atoms on ice (L_{K_ice}). The shape of the lower portion of the K_{diff} matches fairly well with the loss rate. (right) Loss rate per K atom versus altitude showing that at altitudes > 88 km, it becomes less than 50% of the peak values.

midsummer, i.e., above 95 km. The reason for this is two fold: first of all, a greater fraction of the potassium above 92.5 km is in the form of K^+, rather than K, during July compared with May (see Figure 9 in section 5.1). This is because the rate of ionization is greater during midsummer (larger concentration of ambient NO^+ and O_2^+ ions with which K charge transfers). Secondly, the removal of potassium species on the ice clouds affects the whole layer. This is because there is increased downward transport of the metal from above 90 km by vertical eddy diffusion, driven by the increased removal below 90 km.

[17] L_{k_ice} peaks around 88.2 km with values ∼3.8 × 10^{-3} cm^3 s^{-1} in contrast to the difference profile that peaks

at 89 km. Figure 6, right, displays the altitudinal variation of the first-order loss rate of atomic K atom that maximizes around 85 km with a value of ∼2.2 × 10^{-4} s^{-1}, and is more than 41% less efficient in removal of K atoms at altitudes exceeding 87 km. This is consistent with the temporal variation of K densities and SNR shown in Figure 1, which displays an absence of K density below 88 km in contrast to higher altitudes, where the strength of PMSE determines the K densities in the overlap region of the two. We also inferred the loss rate using the early September K densities as the mean unperturbed profile. These calculations revealed similar results as those for the early May period indicating that our selection of unperturbed profiles is justified.
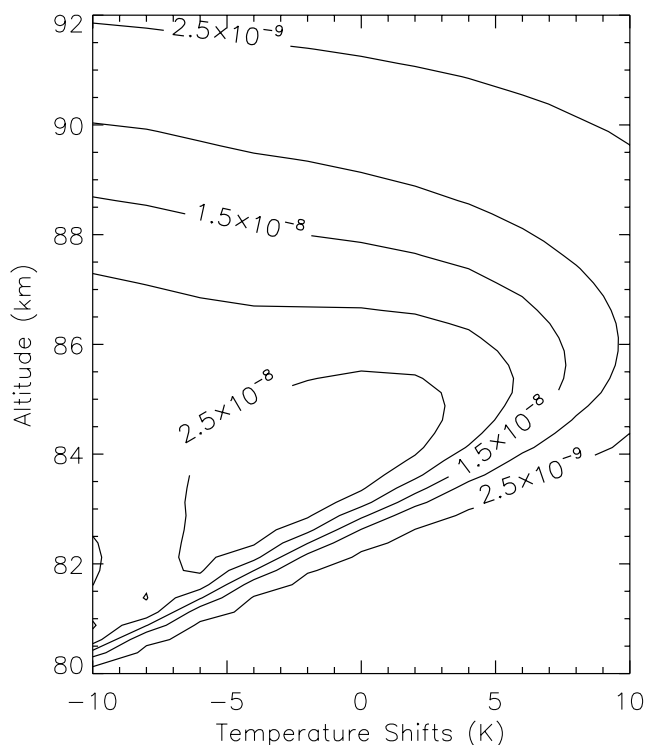
Figure 7. Contour plots of volumetric surface areas of the ice particles [A_{ice}] for different temperature shifts. It is evident that the peak areas remain fairly constant for +4 to −6 K shifts in temperature but are shifted to lower altitudes. Also, for a particular altitude at ∼85 km the variability in [A_{ice}] is ∼±10% for ±5 K perturbations in temperature.

4.2. Sensitivity Studies

[18] Volumetric surface areas simulated with ECARMA clearly depend on atmospheric background parameters. In order to test the sensitivity of our results to changes of atmospheric temperature, water vapor, and eddy diffusion, we have performed a variety of sensitivity studies. The temperature profiles were shifted in steps of 2 K, water vapor was varied in factors of 0.1 while eddy diffusion (K_{zz}) profile was changed drastically by factors of 0.1 and 10, because of the uncertainty involved in the determination of K_{zz}. Considering that the growth of ice particles depends on the saturation ratio (S, defined as the ratio of partial pressure of water vapor to saturation vapor pressure over ice), we investigate in particular the effect of temperature and water vapor on [A_{ice}].

[19] Figure 7 displays the contours of [A_{ice}] corresponding to different shifts in temperature relative to the background profile with other parameters remaining constant. It is evident from the contours of [A_{ice}] that their peak does not vary for a change of +4 to −6 K in the 83–85 km region. However, the peak altitude shifts to lower temperature since the ice particle growth depends on saturation ratio. This study reveals that a change of ±5 K in temperature causes a ±10% change in [A_{ice}] at a fixed altitude.

[20] Figure 8 is similar to Figure 7 except that it shows the variability in [A_{ice}] for various factors in H_2O concentration for a given set of background parameters ($\Delta T = 0$

and Eddy diffusion = 1.0 × K_{zz}). The shift of the peaks to lower altitudes results from increase in saturation ratio that allows ice particles to exist over a wider altitude range. Apart from this, with more water vapor, the ice particles can grow bigger and hence sediment to lower altitudes before they sublime and disappear. Such an increase in water vapor concentration at the bottom of a NLC is seen in satellite measurements [*Summers et al.*, 2001; *McHugh et al.*, 2003] and has been attributed to the freeze drying effect. It is evident from this figure that variations of ±30% in water vapor concentration result in ±10% changes in volumetric surface areas at about 85 km, the peak altitude for [A_{ice}].

5. Modeling the K Layer at 79°N

5.1. Model Description

[21] We now apply a new model of potassium in the mesosphere/lower thermosphere to examine in more detail the competition between heterogeneous removal of K inside an NLC, and the injection of fresh K from both in situ meteoric ablation and transport into the cloud from higher altitudes. The effect of ice clouds on the K layer is also investigated by comparing the modeled layer in May, before the appearance of NLC/PMSE, and in July when ice clouds are present almost continuously.

[22] The model, KMOD, is an extension of the time-resolved model developed for sodium [*Plane*, 2004] and more recently for iron [*Gardner et al.*, 2005; *Plane et al.*, 2004]. The concentrations of the three major gas-phase
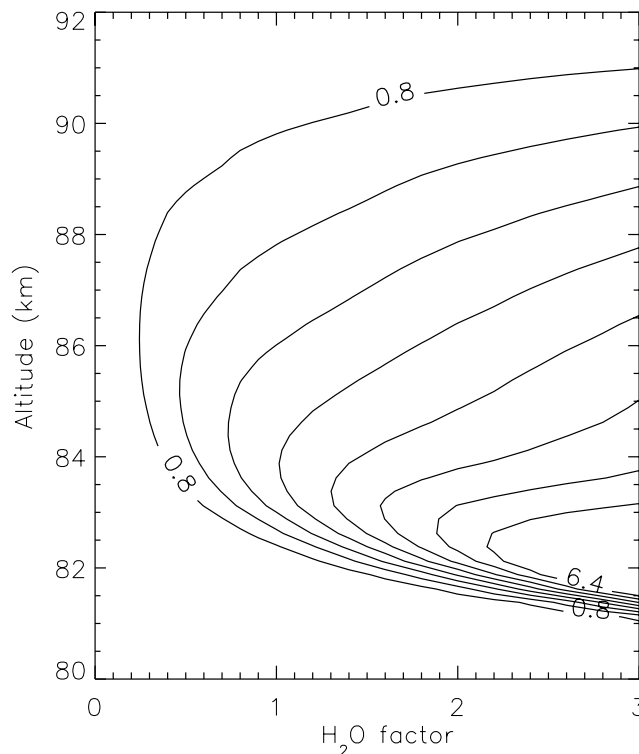
Figure 8. Contours of [A_{ice}] for various water vapor factors that have been multiplied to the background profile to investigate the effect of its variability. A change of ±30% in water vapor concentration corresponds to ±15% variability in [A_{ice}] at 85 km, where [A_{ice}] maximizes.
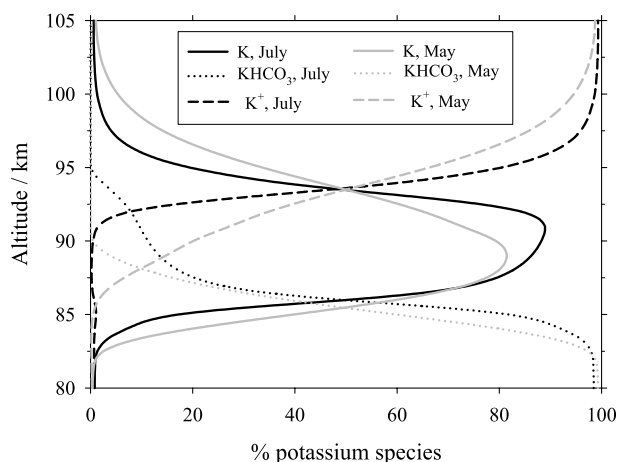
Figure 9. Variation of percent concentration of three major gas-phase potassium species, K, KHCO$_3$, and K$^+$ with altitude, which are determined in KMOD model.

potassium species, K, KHCO$_3$ and K$^+$, are determined in KMOD by full solution of their respective continuity equations. These equations include terms for production of these species by meteoric ablation, and removal by uptake on meteor smoke and ice particles. Figure 9 displays the altitudinal variation of percentage concentration of these species for the core and noncore PMSE seasons at 78°N. Other potassium species, such as KO, KOH and K$^+$ cluster ions (e.g., K$^+$.N$_2$, K$^+$.O, K$^+$.CO$_2$ and K$^+$.H$_2$O), are short-lived intermediates and are therefore treated in chemical steady state. KMOD is 1-dimensional, extending from 65 to 110 km with a height resolution of 0.5 km. The continuity equations are integrated with a 10 minute time step using a time implicit integration scheme [*Shimazaki*, 1985]. The background neutral species (O$_3$, O$_2$, O, H, H$_2$, H$_2$O and CO$_2$) and charged species (NO$^+$, O$_2^+$ and electrons) that control the potassium chemistry are read in every 20 model minutes. Table 1 lists the neutral and ion-molecule reactions involving potassium species that are in the model. The footnotes to the table indicate the source of their respective rate coefficients.

[23] The transport of the metal constituents is assumed to be governed by the same eddy diffusion coefficient K_{zz} up to the turbopause at about 100 km, and above this height by molecular diffusion. Vertical transport by the net vertical wind, w, which arises from the pronounced meridional circulation in the upper mesosphere, is also included. The vertical profiles of K_{zz}, the vertical wind velocity (w) and temperature for July are those shown in Figure 4. It is important to note that for the peak NLC/PMSE season, we have used vertical winds that have been used by *Berger and von Zahn* [2002] to explain the properties of ice particles in the summertime at high latitudes. They calculated the vertical winds by performing a careful tuning of sensitivity parameters in the gravity wave scheme to achieve a good agreement between the model and the summertime observations at the high latitudes. However, in the nonpeak PMSE/NLC season, we are not constrained by the ice particles for the selection of wind profile. K_{zz} and w profiles for May are taken from the NCAR interactive 2-dimensional

global circulation model SOCRATES [*Khosravi et al.*, 2002]. The runs of KMOD shown here were integrated for 40 model days to ensure that the diurnal behavior of the metal layer had stabilized.

[24] Profiles of the pertinent neutral mesospheric species were determined with MESOMOD, also a 1-dimensional model that extends from 65 to 110 km with a height resolution of 0.5 km. It contains a full treatment of the odd oxygen and hydrogen chemistry in the MLT, and has been described in detail previously [*Gardner et al.*, 2005; *Murray and Plane*, 2005a]. MESOMOD was run for 5 model days before a set of diurnal concentration profiles was recorded every 20 minutes for input into KMOD. Profiles of NO$^+$, O$_2^+$ and e$^-$ are input for the appropriate year and time-of-day from the International Reference Ionosphere 2000 model [*Bilitza*, 2003].

[25] The annual average meteoric ablation profile for K is assumed to be the same as that for Na, scaled by an adjustable factor. The Na ablation profile is calculated from an ablation model [*Plane*, 2004] which uses an interplanetary dust particle size and velocity distribution [*McBride et al.*, 1999] derived from the Long Duration Exposure Facility (LDEF) [*Love and Brownlee*, 1991]. The meteor rate in the Arctic during July is 1.3 times higher than in May [*Singer et al.*, 2004], and the same factor was assumed for the relative ablation rate of K between these two months.

[26] Removal of the gas-phase metallic species is modeled by heterogeneous uptake on meteoric smoke particles or PMC ice particles. Meteor smoke has been proposed to form through the recondensation of vaporized meteoroids [*Hunten et al.*, 1980]. The vertical profile of the volumetric surface area of meteor smoke is calculated here using a 1-dimensional model which includes meteoric ablation, polymerization of metal-containing molecules, growth by condensation and coagulation, and removal by sedimentation [*Gabrielli et al.*, 2004; *Plane*, 2004]. All the vaporized meteoroid constituents, including silicon, form oxides or hydroxides that are assumed to condense.

[27] The uptake of potassium species on these smoke particles is likely to be highly efficient and an uptake coefficient of 1.0 is assumed, consistent with a recent laboratory study of K uptake on a silica surface [*Murray and Plane*, 2005b]. Potassium-containing molecules, such as KHCO$_3$, which have large dipole moments, should also stick with high probability. To calculate the removal of potassium species inside an NLC, we use the volumetric surface area determined above (Figure 5d) and an uptake coefficient for K atoms on cubic crystalline ice of 1.0 over the relevant temperature range of 130 to 150 K [*Murray and Plane*, 2005b]. Once again, metallic ions and polar species such as KHCO$_3$ should exhibit highly efficient uptake on H$_2$O-ice surfaces, and are assumed to have uptake coefficients of unity.

5.2. Modeling Results

[28] The best fit to the observations was obtained by setting the annual average K flux to 160 atom cm^{-2} s^{-1}. This corresponds to a relative ablation flux of K to Na of 0.03, which is about 50% of the relative abundance of 0.065 of these elements in chondrites [*Lodders and Fegley*, 1998]. This lower relative ablation flux of K has also been required in a previous model of the K layer, and probably indicates

Table 1. Neutral and Ionic Gas-phase Reactions in the Potassium Model

Number	Reaction	Rate Coefficient[a]	Source[b]
	Neutral Chemistry		
(R1)	$K + O_3 \rightarrow KO + O_2$	$1.15 \times 10^{-9} \exp(-120/T)$	1
(R2)	$KO + O \rightarrow K + O_2$	$2.2 \times 10^{-10} (T/200)^{1/2}$	2
(R3)	$K + O_2(+M) \rightarrow KO_2$	$1.3 \times 10^{-29} (T/200)^{-1.23}$	3
(R4a)	$KO + O_3 \rightarrow KO_2 + O_2$	$1.1 \times 10^{-9} (\exp(-568/T))$	2
(R4b)	$KO + O_3 \rightarrow K + 2O_2$	$6.9 \times 10^{-10} (\exp(-385/T))$	1
(R5)	$KO + O_2(+M) \rightarrow KO_3$	$5.3 \times 10^{-30} (T/200)^{-1}$	2
(R6)	$KO_2 + O \rightarrow KO + O_2$	$5.0 \times 10^{-10} \exp(-940/T)$	2
(R7)	$KO_3 + O \rightarrow K + 2O_2$	$2.5 \times 10^{-10} (T/200)^{1/2}$	2
(R8)	$KO + H_2O \rightarrow KOH + OH$	$4.4 \times 10^{-10} \exp(-650/T)$	4
(R9a)	$KO + H_2 \rightarrow KOH + H$	$1.1 \times 10^{-9} \exp(-1100/T)$	2
(R9b)	$KO + H_2 \rightarrow K + H_2O$	$1.1 \times 10^{-9} \exp(-1400/T)$	2
(R10)	$KO + H \rightarrow K + OH$	$3.0 \times 10^{-10} \exp(-668/T)$	2
(R11)	$KO_2 + H \rightarrow K + HO_2$	$1 \times 10^{-9} \exp(-1000/T)$	2
(R12)	$KOH + H \rightarrow K + H_2O$	$4 \times 10^{-11} \exp(-550/T)$	2
(R13)	$KO + CO_2(+M) \rightarrow KCO_3$	$1.3 \times 10^{-27} (T/200)^{-1}$	2
(R14)	$KCO_3 + O \rightarrow KO_2 + CO_2$	$5 \times 10^{-10} \exp(-1200/T)$	2
(R15)	$KCO_3 + H \rightarrow KOH + CO_2$	$1 \times 10^{-9} \exp(-1000/T)$	4
(R16)	$KOH + CO_2(+M) \rightarrow KHCO_3$	$1.9 \times 10^{-28} (T/200)^{-1}$	2
(R17/-17)	$KHCO_3 + H_2O \leftrightarrow KHCO_3.H_2O$	$2.5 \times 10^{-26} \exp(6240/T)$	5
(R18/-18)	$KHCO_3 + 2H_2O \leftrightarrow KHCO_3.(H_2O)_2$	$1.2 \times 10^{-51} \exp(14260/T)$	5
(R19)	$KHCO_3 + H \rightarrow K + H_2O + CO_2$	$1.1 \times 10^{-9} \exp(-1200/T)$	4
	Ion-Molecule Chemistry		
(R20)	$K + O_2^+ \rightarrow K^+ + O_2$	3.2×10^{-9}	6
(R21)	$K + NO^+ \rightarrow K^+ + NO$	9.4×10^{-10}	6
(R22)	$K^+ + N_2(+M) \rightarrow K^+ \cdot N_2$	$2.3 \times 10^{-30} (T/200)^{-2.39}$	6
(R-22)	$K^+ \cdot N_2(+M) \rightarrow K^+ + N_2$	$2.8 \times 10^{-8} \exp(-1680/T)$	6
(R23)	$K^+ + O_2(+M) \rightarrow K^+ \cdot O_2$	$1.2 \times 10^{-30} (T/200)^{-2.12}$	6
(R-23)	$K^+ \cdot O_2^+(+M) \rightarrow K^+ + O_2$	$1.5 \times 10^{-9} \exp(-820/T)$	6
(R24)	$K^+ + O(+M) \rightarrow K^+ \cdot O^+$	$8.8 \times 10^{-32} (T/200\ K)^{-1.28}$	6
(R-24)	$K^+ \cdot O^+(+M) \rightarrow K^+ + O$	$2.6 \times 10^{-10} \exp(-1800/T)$	6
(R25)	$K^+ + CO_2(+M) \rightarrow K^+ \cdot CO_2$	$1.3 \times 10^{-29} (T/200)^{-2.43}$	6
(R26)	$K^+ + H_2O(+M) \rightarrow K^+ \cdot H_2O$	$3.0 \times 10^{-29} (T/200)^{-2.22}$	6
(R27)	$K^+ \cdot N_2 + O \rightarrow K^+ \cdot O + N_2$	$2.9 \times 10^{-10} (T/200\ K)^{-0.17}$	6
(R-27)	$K^+ \cdot O + N_2 \rightarrow K^+ \cdot N_2 + O$	$2.5 \times 10^{-11} (T/200\ K)^{-0.55}$	6
(R28)	$K^+ \cdot N_2 + CO_2 \rightarrow K^+ \cdot CO_2 + N_2$	$4.8 \times 10^{-10} (T/200\ K)^{-0.88}$	6
(R-28)	$K^+ \cdot CO_2 + N_2 \rightarrow K^+ \cdot N_2 + CO_2$	$2.8 \times 10^{-10} \exp(-2220/T)$	6
(R29)	$K^+ \cdot O_2 + O \rightarrow K^+ \cdot O + O_2$	$2.8 \times 10^{-10} (T/200\ K)^{-0.42}$	6
(R-29)	$K^+ \cdot O + O_2 \rightarrow K^+ \cdot O_2 + O$	$5.0 \times 10^{-10} \exp(-752/T)$	6
(R30)	$K^+ \cdot O + CO_2 \rightarrow K^+ \cdot CO_2 + O$	$7.1 \times 10^{-10} (T/200\ K)^{-0.21}$	6
(R-30)	$K^+ \cdot CO_2 + O \rightarrow K^+ \cdot O + CO_2$	$1.4 \times 10^{-9} \exp(-2200/T)$	6
(R31)	$K^+ \cdot O + H_2O \rightarrow K^+ \cdot H_2O + O$	$7.1 \times 10^{-10} (T/200\ K)^{-1.90}$	6
(R32)	$K^+ \cdot O_2 + N_2 \rightarrow K^+ \cdot N_2 + O_2$	$1.6 \times 10^{-10} (T/200\ K)^{-0.90}$	6
(R-32)	$K^+ \cdot N_2 + O_2 \rightarrow K^+ \cdot O_2 + N_2$	$1.0 \times 10^{-9} \exp(-873/T)$	6
(R33)	$K^+ \cdot O_2 + CO_2 \rightarrow K^+ \cdot CO_2 + O_2$	$1.5 \times 10^{-10} (T/200\ K)^{-1.94}$	6
(R34)	$K^+ \cdot O_2 + H_2O \rightarrow K^+ \cdot H_2O + O_2$	$1.8 \times 10^{-9} (T/200\ K)^{-0.99}$	6
(R35)	$K^+ \cdot N_2 + H_2O \rightarrow K^+ \cdot H_2O + N_2$	$2.4 \times 10^{-9} (T/200\ K)^{-0.45}$	6
(R36)	$K^+ \cdot CO_2 + H_2O \rightarrow K^+ \cdot H_2O + CO_2$	$1.4 \times 10^{-9} (T/200\ K)^{-1.26}$	6
(R37)	$KX^+ + e^- \rightarrow K + X(X = N_2, CO_2, H_2O)$	$1 \times 10^{-6} (T/200)^{-1/2}$	2
	Photochemical Reactions		
(R38)	$KO_2 + hv \rightarrow K + O_2$	4×10^{-3}	2
(R39)	$KOH + hv \rightarrow K + OH$	1×10^{-3}	2
(R40)	$KOH + hv \rightarrow K + OH$	1×10^{-4}	2
(R41)	$K + hv \rightarrow K^+ + e^-$	4×10^{-5}	7

[a]Rate coefficient units: unimolecular, s^{-1}; bimolecular, cm^3 molecule^{-1} s^{-1}; termolecular, cm^6 molecule^{-2} s^{-1}.
[b](1) Measured [*Plane and Helmer*, 1994]; (2) rate coefficient from the analogous sodium reaction [*Eska et al.*, 1999]; (3) measured [*Plane et al.*, 1990]; (4) atmospheric model fit [*Eska et al.*, 1999]; (5) equilibrium constants calculated at the B3LYP/6 − 311 + g(2d,p) level of quantum theory; (6) theory [*Plane et al.*, 2006]; (7) estimate [*Swider*, 1970].

that K ablates slightly less efficiently than Na from molten meteoroids [*Eska et al.*, 1999]. This is consistent with the low abundance ratios of these metals in meteor trails compared to chondrites [*von Zahn et al.*, 2002]. Figure 10 shows the modeled K profiles for early May and July, compared with the lidar observations. The peak heights, absolute densities, and the top- and bottom-scale heights of the layer are satisfactorily modeled in both months. In

particular, the model reproduces the sharp cut-off of the underside of the layer.

[29] One interesting aspect of the conditions in July is the combination of the large eddy diffusion coefficient between 85 and 95 km, and substantial vertical winds with w peaking at 8 cm s^{-1} at 85 km (Figure 4). The vertical wind plays a crucial role in producing the narrow and relatively concentrated K layer above 87 km that is observed. This is because
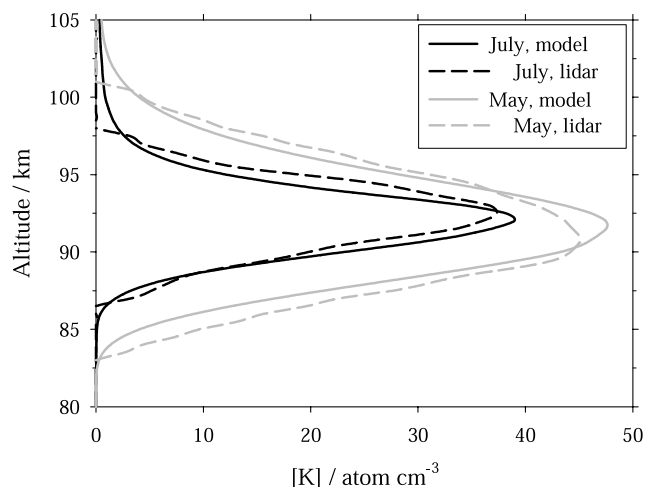
Figure 10. Comparison of modeled and measured K profiles at 79°N in early May (grey lines) and July (black lines).

the KHCO$_3$ which forms below 85 km is displaced upward and converted back to K through photolysis and reaction with H (see Table 1). The importance of w is demonstrated in Figure 11, which shows the broadening effect of reducing w by a factor of 11. Figure 11 also illustrates the effect on the modeled K layer as γ is reduced by a factor of 10 and 100. Even a ten-fold reduction in γ results in an underside of the layer that is clearly too low in altitude by about 3 km, and a substantial increase in the total K layer as less of the ablated K is removed heterogeneously. The lowering of the layer underside occurs because even though there is a significant ice surface area between 85 and 90 km (Figure 11), if γ is small enough then vertical eddy diffusion will transport K down into the NLC from above 90 km. In summary, it appears that the combination of rapid uptake on ice and the large upward wind velocity are required to produce the observed K layer in July.

6.   Discussion

[30]   This work has been prompted by the need to investigate the role of ice particles as an efficient sink for K atoms during summertime at the high latitudes. This question arises from earlier work that tried to explain summertime observations at a midlatitude site (Kühlungsborn) in terms of K chemistry at lower altitudes [*Eska et al.*, 1999]. These authors discussed that the major sink of atomic K is KHCO$_3$ (potassium bicarbonate) and the cold mesopause during summertime should result in a greater concentration of KHCO$_3$. They argued that this process, coupled with an increase in the ratio of O$_3$ to atomic H and O, causes a summertime depletion of K atoms as compared to winter. However, in order to obtain a good agreement between the K lidar observations and model, a scaling factor for the mass flux (also referred to as ablation efficiency) of 0.05 was required. The uncertainty in the scaling factor of the ablation efficiency can probably be reduced by quantifying various sink processes. This led us to evaluate the loss rate of the K atoms on ice, which is a function of volumetric surface area of ice particles [A$_{ice}$] and unperturbed K density.

[31]   We determined [A$_{ice}$] using an empirical method that combined microphysical models (ECARMA) and PMSE/NLC data. This study revealed [A$_{ice}$] to peak around 85 km with values $\sim 2 \times 10^{-8}$ cm^{-1}. One of the interesting results is that the peak [A$_{ice}$] is 5 times larger than the volumetric surface area above 89 km. This results in the loss rate of K atoms on ice, which is a function of [A$_{ice}$] and the unperturbed K density profile, maximizing around 88 km with values close to 3.8×10^{-3} atom cm^{-3} s^{-1}. This is about a factor of 10 greater than the meteoric flux rates which were used in the earlier modeling work to explain the seasonal variation of the potassium layer at midlatitudes [*Eska et al.*, 1999]. The contribution of ice particles as one of the major sink mechanisms and the transport due to the presence of strong vertical winds in the K density model has resulted in the use of an annual K flux of 160 atom cm^{-2} s^{-1}, which is necessary for obtaining a best fit between observations and model. This implies a low ablation flux of K relative to other metals like Na and is consistent with the differential ablation theory [*McNeil et al.*, 2002].

[32]   It is important to note that our calculations of [A$_{ice}$] use microphysical ice models that assume particles to be of spherical shape. However, depolarization methods suggest that ice particles might be elongated with length over diameter ratio of at least 2.5 [*Baumgarten et al.*, 2002]. This results in an increase in surface area by 25% relative to a sphere of equal volume. Hence this uncertainty in the particle shape would result in a surface area enhancement and consequently increase in the loss rate magnitude.

[33]   We also performed a sensitivity study to investigate the variability of [A$_{ice}$] on background parameters. This work suggested that peak [A$_{ice}$] strongly increases with an increase in water vapor concentration whereas the temperature decrease results in minor effects.
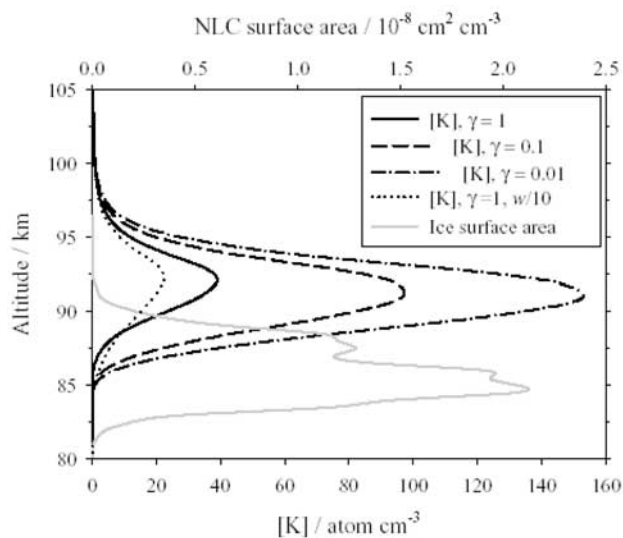
Figure 11. Modeled K profiles at 79°N during July when the uptake coefficient of K on ice, γ, is set to 1, 0.1, and 0.01 and for the case where $\gamma = 1$ but the vertical wind velocity, w, is reduced by a factor of 10. The grey line shows the volumetric surface area of ice particles used in the model.

[34] We tried to estimate the [A_{ice}] for the beginning and end season of PMSE by using the climatological conditions prevalent at 78°N during that period. However, ECARMA did not produce any ice particles for the mean background conditions but weak layers were formed when temperatures were decreased to −6 K relative to the mean temperature profile from that period. This implies that during the start and end of PMSE season, ice particles occur only in the extreme events of gravity waves that perturb the background temperature. This is consistent with the small occurrence rate of PMSE during the early and late part of the PMSE season.

7. Summary and Conclusions

[35] Experimental and modeling efforts indicate that the presence of ice particles and strong vertical winds control the shape of the K layer at high latitudes. A novel approach has been developed for the determination of volumetric surface area of ice particles by combining PMSE and NLC data from Svalbard (78°N) along with microphysical model results. A new time-resolved K model reproduces the early May and July profiles that compare well with lidar observations at Spitsbergen. In future, an extension of this work should be done to obtain the loss rates at nonpeak PMSE season which will probably facilitate the full development of the model. Also, the observations of K densities from other sites where POR (PMSE occurrence rate) < 100% can shed more light on the interaction process.

References

Balsley, B. B., and M. Huaman (1997), On the relationship between seasonal occurrence of northern hemispheric polar mesosphere summer echoes and mean mesopause temperatures, *J. Geophys. Res.*, *102*, 2021–2024.

Baumgarten, G., K. H. Fricke, and G. von Cossart (2002), Investigation of the shape of noctilucent cloud particles by polarization lidar technique, *Geophys. Res. Lett.*, *29*(13), 1630, doi:10.1029/2001GL013877.

Berger, U., and U. von Zahn (2002), Icy particles in the summer mesopause region: Three-dimensional modeling of their environment and two-dimensional modeling of their transport, *J. Geophys. Res.*, *107*(A11), 1366, doi:10.1029/2001JA000316.

Bilitza, D. (2003), International reference ionosphere 2000: Examples of improvements and new features, *Adv. Space Res.*, *31*(3), 757–767.

Blix, T. A., M. Rapp, and F.-J. Lübken (2003), Relations between small scale electron number density fluctuations, radar backscatter, and charged aerosol particles, *J. Geophys. Res.*, *108*(D8), 8450, doi:10.1029/2002JD002430.

Chilson, P. B., E. Belova, M. Rietveld, S. Kirkwood, and U.-P. Hoppe (2000), First artificially induced modulation of PMSE using the EISCAT heating facility, *Geophys. Res. Lett.*, *27*, 3801–3804.

Cho, J. Y. N., and J. Röttger (1997), An updated review of polar mesosphere summer echoes: Observation, theory, and their relationship to noctilucent clouds and subvisible aerosols, *J. Geophys. Res.*, *102*, 2001–2020.

Cho, J. Y. N., T. M. Hall, and M. C. Kelley (1992), On the role of charged aerosols in polar mesosphere summer echoes, *J. Geophys. Res.*, *97*, 875–886, doi:10.1029/91JD02836.

Eska, V., U. von Zahn, and J. M. C. Plane (1999), The terrestrial potassium layer (75–110 km) between 71°S and 54°N: Observations and modeling, *J. Geophys. Res.*, *104*, 17,173–17,186.

Gabrielli, P., et al. (2004), Meteoric smoke fallout over the Holocene revealed by iridium and platinum in Greenland ice, *Nature*, *432*(7020), 1011–1014.

Gardner, C. S., J. M. C. Plane, W. Pan, T. Vondrak, B. J. Murray, and X. Chu (2005), Seasonal variations of the Na and Fe layers at the South Pole and their implications for the chemistry and general circulation of the polar mesosphere, *J. Geophys. Res.*, *110*, D10302, doi:10.1029/2004JD005670.

Hocking, W. K., and J. Röttger (1997), Studies of polar mesosphere summer echoes over EISCAT using calibrated signal strengths and statistical parameters, *Radio Sci.*, *32*, 1425–1444.

Hoffmann, P., M. Rapp, A. Serafimovich, and R. Latteck (2005), On the occurrence and formation of multiple layers of polar mesosphere summer echoes, *Geophys. Res. Lett.*, *32*, L05812, doi:10.1029/2004GL021409.

Hunten, D. M., R. P. Turco, and O. B. Toon (1980), Smoke and dust particles of meteoric origin in the mesosphere and stratosphere, *J. Atmos. Sci.*, *37*, 1342–1357.

Kelley, M. C., D. T. Farley, and J. Röttger (1987), The effect of cluster ions on anomalous VHF backscatter from the summer polar mesosphere, *Geophys. Res. Lett.*, *14*, 1031–1034.

Khosravi, R., G. Brasseur, A. Smith, D. Rusch, S. Walters, S. Chabrillat, and G. Kockarts (2002), Response of the mesosphere to human-induced perturbations and solar variability calculated by a 2–D model, *J. Geophys. Res.*, *107*(D18), 4358, doi:10.1029/2001JD001235.

Körner, U., and G. R. Sonnemann (2001), Global three-dimensional modeling of the water vapor concentration of the mesosphere-mesopause region and implications with respect to the noctilucent cloud region, *J. Geophys. Res.*, *106*, 9639–9652.

Lodders, K., and B. Fegley (1998), *The Planetary Scientist's Companion*, p. 371, Oxford Univ. Press, New York.

Love, S. G., and D. E. Brownlee (1991), Heating and thermal transformation of micrometeoroids entering the Earth's atmosphere, *Icarus*, *89*, 26–43.

Lübken, F.-J. (1997), Seasonal variation of turbulent energy dissipation rates at high latitudes as determined by in situ measurements of neutral density fluctuations, *J. Geophys. Res.*, *102*, 13,441–13,456.

Lübken, F.-J. (1999), Thermal structure of the Arctic summer mesosphere, *J. Geophys. Res.*, *104*, 9135–9149.

Lübken, F.-J., and J. Höffner (2004), Experimental evidence for ice particle interaction with metal atoms at the high latitude summer mesopause region, *Geophys. Res. Lett.*, *31*, L08103, doi:10.1029/2004GL019586.

Lübken, F.-J., and A. Müllemann (2003), First in situ temperature measurements in the summer mesosphere at very high latitudes (78°N), *J. Geophys. Res.*, *108*(D8), 8448, doi:10.1029/2002JD002414.

Lübken, F.-J., J. Höffner, C. F. Begemann, A. Müllemann, M. Zecha, and J. Röttger (2002), Mesospheric layers and temperatures at Spitsbergen, 78°N, *Mem. Br. Astron. Assoc.*, *45*, 97–114.

Lübken, F.-J., M. Zecha, J. Höffner, and J. Röttger (2004), Temperatures, polar mesosphere summer echoes, and noctlilucent clouds over Spitsbergen (78°N), *J. Geophys. Res.*, *109*, D11203, doi:10.1029/2003JD004247.

McBride, N., S. F. Green, and J. A. M. McDonnell (1999), Meteoroids and small sized debris in Low Earth Orbit and at 1 Au: Results of recent modelling, *Adv. Space Res.*, *23*(1), 73–82.

McHugh, M., M. Hervig, B. Magill, R. E. Thompson, E. Remsberg, J. Wrotny, and J. Russell III (2003), Improved mesospheric temperature, water vapor and polar mesospheric cloud extinctions from HALOE, *Geophys. Res. Lett.*, *30*(8), 1440, doi:10.1029/2002GL016859.

McNeil, W. J., E. Murad, and J. M. C. Plane (2002), Models of meteoric metals in the atmosphere, in E. Murad and I. P. Williams, pp. 265–287, Cambridge Univ. Press, New York.

Murray, B. J., and J. M. C. Plane (2005a), Modelling the impact of noctilucent cloud formation on atomic oxygen and other minor constituents of the summer mesosphere, *Atmos. Chem. Phys.*, *5*, 1027–1038.

Murray, B. J., and J. M. C. Plane (2005b), Uptake of Fe, Na and K atoms on low-temperature ice: Implications for metal atom scavenging in the vicinity of polar mesospheric clouds, *Phys. Chem. Chem. Phys.*, *7*, 3970–3979.

Plane, J. M. C. (2003), Atmospheric chemistry of meteoric metals, *Chem. Rev.*, *103*, 4963–4984.

Plane, J. M. C. (2004), A time-resolved model of the mesospheric Na layer: Constraints on the meteor input function, *Atmos. Chem. Phys.*, *4*, 627–638.

Plane, J. M. C., and M. Helmer (1994), Laboratory studies of the chemistry of meteoric metals, in *Research in Chemical Kinetics*, edited by G. Hancock and R. G. Compton, pp. 313–367, Elsevier, New York.

Plane, J. M. C., B. Rajasekhar, and L. Bartolotti (1990), Kinetic study of the reaction K + O$_2$ + N$_2$, K + O$_2$ + He from 250 K to 1103 K, *J. Phys. Chem.*, *94*(10), 4161–4167.

Plane, J. M. C., B. J. Murray, X. Chu, and C. S. Gardner (2004), Removal of meteoric iron on polar mesospheric clouds, *Science*, *304*, 426–428.

Plane, J. M. C., R. J. Plowright, and T. G. Wright (2006), A theoretical study of the ion-molecule chemistry of K$^+$.X complexes (X = O, O$_2$, N$_2$, CO$_2$, H$_2$O): Implications for the upper atmosphere, *J. Phys. Chem. A.*, *110*(9), 3093–3100, doi:10.1021/jp054416g.

Rapp, M., and F.-J. Lübken (2000), Electron temperature control of PMSE, *Geophys. Res. Lett.*, *27*, 3285–3288.

Rapp, M., and F.-J. Lübken (2001), Modelling of particle charging in the polar summer mesosphere: Part 1. General results, *J. Atmos. Sol. Terr. Phys.*, *63*, 759–770.

Rapp, M., and F.-J. Lübken (2003), On the nature of PMSE: Electron diffusion in the vicinity of charged particles revisited, *J. Geophys. Res.*, *108*(D8), 8437, doi:10.1029/2002JD002857.

Rapp, M., and F.-J. Lübken (2004), Polar mesosphere summer echoes (PMSE): Review of observations and current understanding, *Atmos. Chem. Phys.*, *4*, 2601–2633.

Rapp, M., and G. E. Thomas (2006), Modeling the microphysics of mesospheric ice particles–Assessment of current capabilities and basic sensitivities, *J. Atmos. Sol. Terr. Phys*, *68*(7), 715–744.

Rapp, M., F.-J. Lübken, P. Hoffmann, R. Latteck, G. Baumgarten, and T. A. Blix (2003), PMSE dependence on aerosol charge number density and aerosol size, *J. Geophys. Res.*, *108*(D8), 8441, doi:10.1029/2002JD002650.

Seele, C., and P. Hartogh (1999), Water vapor of the polar middle atmosphere: Annual variation and summer mesosphere conditions as observed by ground-based microwave spectroscopy, *Geophys. Res. Lett.*, *26*, 1517–1520.

She, C. Y., B. P. Williams, P. Hoffmann, R. Latteck, G. Baumgarten, J. D. Vance, J. Fiedler, P. Acott, D. C. Fritts, and F.-J. Lübken (2006), Simultaneous observation of sodium atoms, NLC and PMSE in the summer mesopause region above ALOMAR, Norway (69°N, 12°E), *J. Atmos. Sol. Terr. Phys.*, *68*(1), 93–101, doi:10.1016/j.jastp.2005.08.014.

Shimazaki, T. (1985), *Minor Constituents in the Middle Atmosphere*, Springer, New York.

Singer, W., U. von Zahn, and J. Weiss (2004), Diurnal and annual variations of meteor rates at the Arctic Circle, *Atmos. Chem. Phys.*, *4*, 1355–1363.

Summers, M. E., R. R. Conway, C. R. Englert, D. E. Siskind, M. H. Stevens, J. M. Russell III, L. L. Gordley, and M. J. McHugh (2001), Discovery of water vapor layer in the Arctic summer mesosphere: Implications for polar mesospheric clouds, *Geophys. Res. Lett.*, *28*(18), 3601–3604.

Swider, W. (1970), Ionic reactions for meteoric elements, *Ann.. Geophys.*, *26*, 595–599.

Thomas, G. E. (1991), Mesospheric clouds and the physics of the mesopause region, *Rev. Geophys.*, *29*, 553–575.

von Zahn, U., J. Höffner, and W. J. McNeil (2002), Meteor trails as observed by lidar, in *Meteors in the Earth's Atmosphere*, edited by E. Murad and I. P. Williams, pp. 149–187, Cambridge Univ. Press, New York.

————————————

J. Höffner, F.-J. Lübken, M. Rapp, and M. Zecha, Institute of Atmospheric Physics, Schloss Strasse 6, Kühlungsborn 18225, Germany.

J. M. C. Plane, School of Chemistry, University of Leeds, Woodhouse Lane, Leeds LS2 9JT, UK.

S. Raizada, Arecibo Observatory, HC-03 Box 53995, Arecibo 00612, Puerto Rico, USA. (shikha@naic.edu)